Decoding Multiple Interfering Signals in a Macroscopic Air-based Molecular Communication System

Rebecca Corinna Pampu
TU Berlin, Germany
r.pampu@tu-berlin.de

Lukas Stratmann
TU Berlin, Germany
stratmann@ccs-labs.org

Jorge Torres Gómez
TU Berlin, Germany
torres-gomez@ccs-labs.org

Falko Dressler
TU Berlin, Germany
dressler@ccs-labs.org

ABSTRACT

Molecular communication (MC) prevails as a preferred scheme in environments where electromagnetic waves are not feasible such as tunnels, mines, or pipes. Air-based molecular communication (MC) promises an increased data rate compared to fluid-based implementations, particularly for distances of a few meters. In this paper, we investigate the communication performance of a 2-sender-1-receiver transmission model. We propose a mechanism with low complexity that allows to decode multiple overlaying signals modulated using On-Off-Keying (OOK). In particular, our receiver interprets the signal as an Quadrature Concentration Shift Keying (QCSK) modulated waveform. We conducted experiments to study the impact of parameter changes, especially concerning a distance offset between the emitters and the receiver and the timing offset on the emitter's side. The key metric used is the bit error rate (BER). Our results indicate that an adequate parameter setup and sampling point allows achieving a quasi-error-free transmission.

CCS CONCEPTS

• **Computing methodologies** → **Modeling methodologies**; • **Networks** → **End nodes**.

KEYWORDS

Air-based Molecular Communication, Interference, Molecular Communications, Simulation, Synchronization

ACM Reference Format:
Rebecca Corinna Pampu, Lukas Stratmann, Jorge Torres Gómez, and Falko Dressler. 2023. Decoding Multiple Interfering Signals in a Macroscopic Air-based Molecular Communication System. In *The 10th ACM International Conference on Nanoscale Computing and Communication (NANOCOM '23), September 20–22, 2023, Coventry, United Kingdom.* ACM, New York, NY, USA, 6 pages. https://doi.org/10.1145/3576781.3608722

NANOCOM '23, September 20–22, 2023, Coventry, United Kingdom

ACM ISBN 979-8-4007-0034-7/23/09…$15.00
https://doi.org/10.1145/3576781.3608722

1 INTRODUCTION

Molecular communication (MC) has been gaining attention over the last years and macroscopic MC is expected to be potentially part of next generation wireless networks [10]. It poses a promising alternative in wireless communication for industrial or other RF-unfriendly environments where transmissions based on electromagnetic waves would suffer too high of a propagation loss (e.g., tunnels, mines, pipes) [15]. Macroscopic MC can be used, e.g., for detection of corrosion in pipelines or the detection of leakages in confined environments.

In MC, information is encoded via the concentration, type, and/or release time of molecules [12] emitted or sprayed into a liquid or gaseous medium as transmission channel [4, 9]. Molecules act as information carriers while modulating specific physical and/or chemical properties to enable an information channel. Various testbeds illustrate the affordability of conceiving air and liquid-based channels as MC links [4, 8, 11]. Solutions include implementing air-based links using alcohol molecules in the range of 2–4 m [8]. Transceivers for emitting and detecting fluorescent dyes are also reported to achieve longer distances in liquid-based environments as long as 15 m [1] and in more realistic channels with obstacles where turbulence is produced [3]. Furthermore, trying to reach higher bitrates, the experiments reported by Bhattacharjee et al. [4] show that air-based MC might have a higher transmission rate than comparable fluid-based transmission in the distance range of meters.

Further advancing our previous work in [4], we reduce the overall need for hardware components and memory capacity in the receiver while improving the transmission rate. While our initial experiment uses only one transmitter (Tx) and one receiver (Rx) [4], using two Tx to the same Rx would potentially reduce the need for relay nodes. This setup finds applicability in a large-scale application such as a tunnel of hundreds to thousands of meters where sensors are located every few meters. Additionally, the receiver hardware is reduced from a camera to a simple photodetector. Our 2-Tx-1-Rx architecture can potentially double the received bit-rate, when both Tx are sending simultaneously.

In this paper, we investigate the communication parameters for enabling a quasi-error-free transmission between two Tx and one Rx. We model the transmission from two emitters using On-Off-Keying (OOK) modulation, while the receiver implements a Quadrature Concentration Shift Keying (QCSK) demodulator. Specifically, we evaluate the impact of the relative distance between emitters and receivers on the communication performance, as well as the

transmission timing offset.[1] This is achieved by reconstructing the messages using the molecule concentration differences at the receiver due to distance offset and timing offsets.

Our main contributions can be summarized as follows:

- We study the impact of interference between multiple OOK signals in an air-based MC system;
- we present a 2-Tx-1-Rx architecture exploiting the physical characteristics leading to the resulting QCSK signal; and
- we study the performance of our system in depth and show that a quasi-error-free transmission is possible.

2 RELATED WORK

Discussions regarding the communication settings for two Tx sharing the same communication channel focus on the induced co-channel interference and the impact of inter-symbol interference (ISI) [13]. Examining the possibility of collision avoidance, a quick description of usual mitigation schemes is interesting: For example, in wireless body area networks adaptive schemes exist, which reduce the power levels or data rate as soon as interference is detected [17]. This would require a Tx structure that is able to detect the interference, thereby increasing implementation costs.

Further suggested methods in the field of MC are on the one hand to use Molecular Shift Keying (MoSK) as modulation scheme, using different type of molecules for each Tx [2]. However, the components shall be as simple and mass-producible as possible. On the other hand, installing medium access schemes like channel reservation or time-division multiplexing seems feasible [2]. However, a reactive approach is impossible and continuously dividing the transmission time between both senders would unnecessarily halve the data rate when just one sender is transmitting.

MoSK has proven to be a good solution for ISI mitigation [6], and an approach without the complexity of different types of molecules has been presented [16]. On the Tx-side, Molecular Transition Shift Keying (MoTSK) was employed as the modulation scheme, where the ISI was utilized for benefiting the communication performance instead of avoiding it [16]. This approach requires increased memory and computation on the transmitter side but is a feasible solution to reduce ISI in the communication link. Similar to a MoSK-based scheme, this could be an interesting approach for future adaptations with a complexity trade-off.

One of the key proactive mitigation schemes in MC is to increase the distance from the interferer, as the amplitude of the signal will drop [13]. This property, which we also observed in previous experiments, is used as an advantage in this research with a non-symmetric distance between each Tx and the Rx. The different power levels of the two Tx passively allow the two OOK-Tx modulations to be decoded as a single QCSK at the Rx side (further details in Section 4).

The key-challenge for such a design results in deriving a proper decoding threshold at the receiver. Damrath and Hoeher [5] propose an adaptive threshold setting depending on the previous bit. Furthermore, Tepekule et al. [16] argue that an empirical instead of an analytical approach to determine the threshold is more cost-intensive. However, in the specific use case of two fixed Tx and one Rx locations, the thresholds do not need to be updated very often and can be calculated efficiently in a limited training-sequence.

[1] We refer the reader to [14] for further details on the implementation.

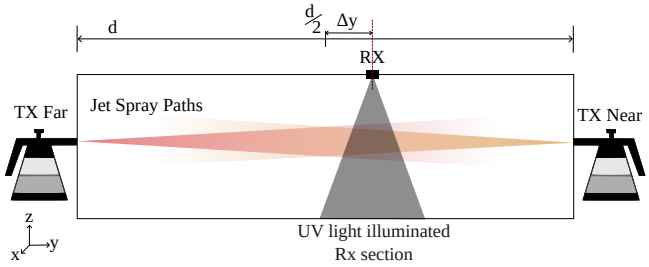

Figure 1: Schematic of 2-Tx-1-Rx layout with offset

3 SYSTEM MODEL

Our system model mimics testbed-based experiments in our previous work [4]. The testbed comprises a water-uranine-based solution with a single pair of transmitter and receiver. The solution is injected by the *Gloria Type 89* industrial sprayer in jet-mode into a dark tube. The released molecules are detected via a camera and the ultraviolet (UV)-light composition.

In the new layout that we use in this paper, two identical sprayers are positioned on opposite sides of the receiver as depicted in Fig. 1. In order to reduce the complexity of the hardware, the Rx is replaced by a photodetector, while still assuming the same detection angle and frame rate. Thus, only the light intensity value (LIV) can be recorded and not a direction of movement over image frames. In the simulation, every molecule-object in the receiver's area increases the LIV by 1. This has to be fitted to the specific receiver in an adjusted physical testbed to account for overlap and light saturation.

We model the mobility of molecules accounting for the sprayer geometry and physical channel effects. As reported in [4], travelling molecules are described by two random variables concerning direction (β) and a speed (γ) as

(i) a uniformly distributed rotational component around the x- and z-axis $\alpha \in [0, 2\pi]$ with a normal distribution $\beta = N(\mu = 0, \sigma_{dist} = 1.55)$ over the radius
(ii) a longitudinal normal distribution $\gamma = N(\mu = v_{\text{mean}} = 12.82\,\text{m/s}, \sigma_{v_y} = 3\,\text{m/s})$

With (i), it is possible to model the cone-shape of the sprayer ray (see Fig. 1) also accounting for the reduced detected power over distance, and with (ii), we account for the spread in arrival time. This spread is due to air drag and gravity on differently sized droplets and the not instantaneous valve-shutting of the sprayer resulting in trailing emission.

In the 3-D MC channel, each molecule i moves with a constant velocity vector computed as

$$\vec{v}_i = \begin{pmatrix} v_{x,i} \\ v_{y,i} \\ v_{z,i} \end{pmatrix} = \gamma_i \cdot \begin{pmatrix} \sin(\beta_i) \cdot \sin(\alpha_i) \\ \cos(\beta_i) \\ \sin(\beta_i) \cdot \cos(\alpha_i) \end{pmatrix}. \quad (1)$$

The transmission channel itself does not have a flow and is not considered to impact the molecule movement. Furthermore, this velocity caused by the sprayer is dominant when compared to diffusion effects or air-drag and gravity. Thus, we model the molecules' mobility in the MC channel with constant speed (as given by Eq. (1))

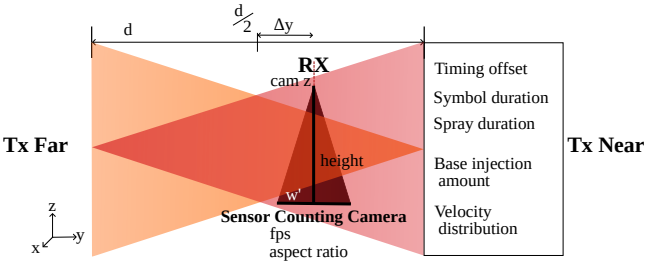

Figure 2: Simulation Appearance

and following the trajectory specified by the velocity vector $\vec{v}_i$. The particle's position $\vec{p}_{i,n}$ at time step n is updated with its previous position $\vec{p}_{i,n-1}$, the velocity $\vec{v}_i$ vector, and the time step size Δt_{sim} as

$$\vec{p}_{i,n} = \vec{p}_{i,n-1} + \vec{v}_i \cdot \Delta t_{\text{sim}}, \tag{2}$$

where the initial position for each particle is at the coordinates specified by each emitter sprayer. Our mobility model given by Eq. (2) does not consider bounds like tube walls. We assume that the droplets adhere to the tube wall and do not re-enter the Rx section when draining.

The receiver section is fully described by the Rx z-position (assumed as "up" with respect to the Tx). The receiver will be able to read the number of molecules located in a pyramid-shaped region, acting as a droplet-counting camera sensor, with its location denoted as cam z in Fig. 2. The receiver observation region is modeled as a pyramid with height as the tube diameter and the width of the view as seen at the bottom of the tube as the parameter w', cf. Fig. 2. The Rx records discretely (as image frames).

For transmissions, we model the spraying of uranine-solution via OOK by both Tx. To encode and decode the message based on the LIV camera, both Tx and the Rx are assumed to have perfect synchronization. The used training sequence for transmissions consists of 144 bit to cover all possible combinations of subsequent symbols. After the thresholds are calculated from the LIVs, any sequence can be demodulated (further details in Section 4).

We implemented this system model in the Rogona simulator accounting for the release and mobility of particles, as well as for the (de-)modulation schemes.[2] The Rogona simulator takes a simulation configuration file and a reconstruction configuration file to modulate and demodulate a specified message.

In the simulator, timing offsets, power, symbol duration, and spray duration, among others, can be set as part of a configuration file. Beforehand, we define the Tx–Tx distances (labelled as d in Fig. 1) and the respective symbol durations. Based on the examined Tx–Rx distances in [4] (58, 88, 118, 148, and 178 cm), the simulator models the distance range of 120–320 cm. This way, both Tx–Rx distances stay within the already examined range. We explicitly include 120 cm in this group, because early experiments have shown that the original symbol duration $t_{\text{sym}} = 50$ ms could only realistically lead to a reliable transmission at $d = 160$ cm.[3]

[2]Rogona is based on our Pogona simulator [7]. We re-implemented the simulator in Rust, including some architecture changes, which provided a significant improvement in execution performance. We provide open access to Rogona at https://github.com/tkn-tub/rogona.

[3]Due to ISI effects and an increased standard deviation of LIVs per code, the channel impulse responses (CIRs) would be indistinguishable at any image frame.

Although the simulator itself is not restricted to any distance d and symbol duration t_{sym} pairs, we recommend the following assignments:

$$t_{\text{sym}} = 50\,\text{ms} \rightarrow d \in [120\,\text{cm},\ 160\,\text{cm}]$$
$$t_{\text{sym}} = 75\,\text{ms} \rightarrow d \in [160\,\text{cm},\ 200\,\text{cm},\ 240\,\text{cm},\ 280\,\text{cm}]$$
$$t_{\text{sym}} = 100\,\text{ms} \rightarrow d \in [280\,\text{cm},\ 320\,\text{cm}]$$

The spray duration (time of injecting molecules at the beginning of the symbol duration) stays at 20 ms.

4 COMMUNICATION PROTOCOL/STRATEGY

For the communication strategy, we account for the case when both messages are being sent simultaneously in the 2-Tx-1-Rx architecture (see Fig. 1). As a consequence, collisions on the shared communication channel are unavoidable, but we will devise a strategy to decode the emissions at the receiver properly. Specifically, we investigate mainly two parameters:

(i) Distance offset Δy: The Rx is shifted from the middle towards one of the Tx, as shown in Fig. 1.
(ii) Timing offset Δt: The Tx can send delayed with respect to the symbol start.

Option (i) utilizes the decreasing LIV with increasing distance, while option (ii) uses the relative position of the CIRs to each other to reveal a good sampling point.

To illustrate the impact of the distance offset, let's assume the receiver is located in the exact middle between both transmitters ($\Delta y = 0$ in Fig. 2). Upon the reception of a '1' from just one Tx, the receiver will not be able to identify, which of the two transmitters emitted the particles. However, this uncertainty in identifying the emitter can be reduced as we locate the receiver with some offset distance from the center. In this case, the emission of a '1' can be distinguishable due to the observed amplitude level when coming from the emitter on the left or to the right. The different distances between the two emitters to the receiver will change the amplitudes and shapes of the CIRs. Due to an in-/decreased travel distance the peak amplitudes of the LIVs will drift apart in the time-domain.

As for the timing offset, performing emissions with some relative delay between the two Tx will also shift the location of the peak amplitude with time and without changing the CIR shape, as perceived by the Rx. Even when the receiver is located at the center, the emitter with a delay in transmissions can be distinguished from the other Tx as its LIV will be still higher/lower compared to the emitter without delay.

Using the time and/or distance offset parameters, we artificially produce four different concentration levels on the Rx side at a certain sampling point. For instance, at the Rx, the LIV detector will observe various CIRs as depicted in Fig. 3, according to each possible bit-pair. For better readability and comprehensiveness these symbols are named as

$$\text{Tx}_{\text{far}} \xrightarrow{'1'} \xleftarrow{'1'} \text{Tx}_{\text{near}} \rightarrow \textbf{H}\text{igh (H)}$$
$$\text{Tx}_{\text{far}} \xrightarrow{'1'} \xleftarrow{'0'} \text{Tx}_{\text{near}} \rightarrow \textbf{F}\text{ar only (F)}$$
$$\text{Tx}_{\text{far}} \xrightarrow{'0'} \xleftarrow{'1'} \text{Tx}_{\text{near}} \rightarrow \textbf{N}\text{ear only (N)}$$
$$\text{Tx}_{\text{far}} \xrightarrow{'0'} \xleftarrow{'0'} \text{Tx}_{\text{near}} \rightarrow \textbf{L}\text{ow (L)}$$

By choosing one sampling point per symbol, the memory requirements on the Rx are minimized. The sampling point is the

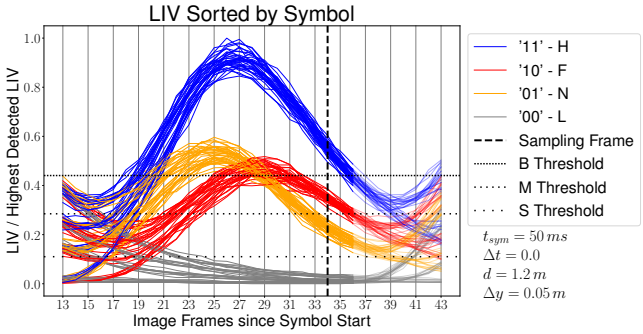

Figure 3: Training-sequence

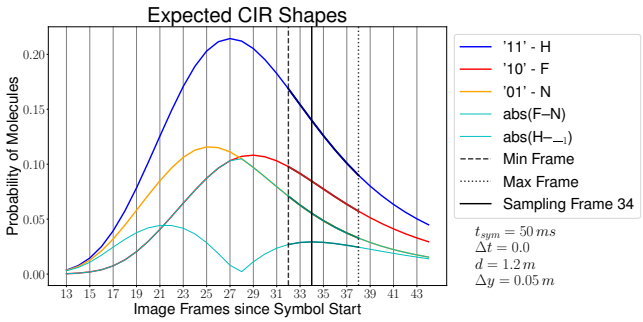

Figure 4: CIR estimate and frame selection

image frame in which we try to maximize the absolute differences between the symbols. We calculate the difference from the estimate of the CIR. The CIR is estimated by the probability of molecules in the Rx section when an image frame is recorded. This probability directly correlates with the LIVs, so that a maximum difference between the probabilities will result in distinguishable symbols, see frame 34 in Figures 3 and 4.

The frame selection works based on the following heuristics:

(i) A minimum and maximum frame is defined for ISI avoidance. The ISI can be observed in the overlapping symbols between frame 13 and 19 at the beginning of the depicted image frames in Fig. 3 and between frame 36 and 43 at the end of the image frames. Therefore, the selection is restricted to the frames 32 to 38 for this case, see Fig. 4. The calculation of minimum and maximum frame is based on the travel times of molecules with different velocities from Tx to Rx.

(ii) Between the min and max frames, two absolute differences are considered. On the one hand

$$|F - N|, \tag{3}$$

to distinguish between $\mathrm{Tx}_{\mathrm{far}}$ and $\mathrm{Tx}_{\mathrm{near}}$ in case they are not simultaneously sending a '1'. On the other hand

$$|H - \_1|, \tag{4}$$

to distinguish the symbols when they are simultaneously sending a '1'. The notation $\_1$ represents the symbol with the higher expected LIV out of F and N at the image frame, see the green curve in Fig. 4. We need to consider $\_1$, because the symbol's LIVs will always be (closest to) interfering with the LIV range of H.

(iii) Both differences in Equations (3) and (4) should be maximized. The decision is a trade-off two-dimensional maxfind. Due to a discrete detection as image frames, the possibilities are finite and the values can be processed as two arrays. The index of the maximum value per array is looked up and checked as:
- If the indices are equal, we select the frame corresponding to the index as sampling frame.
- If they are adjacent, we select the frame corresponding to the index of the lower value.
- If the maximum value of one difference is significantly smaller than the maximum of the other difference, the frame corresponding to the index of the lower value is immediately selected.
- Otherwise, their values are set to 0 and the process is repeated.

Upon the frame selection, we determine three thresholds, as depicted in Fig. 3 with B, M, and S threshold:

Big threshold (B) between H and $\_1$
Medium threshold (M) between F and N
Small threshold (S) between $\_2$ and L

The notation $\_2$ refers to F or N depending on which one has the lower LIV at the sampling frame.

The threshold setting works as follows:

(i) Both Tx send a training-sequence, and the Rx knows the order of symbols.

(ii) At the Rx we identify the respective LIV samples with the emitted symbol and order them by size. As a result we will have four collections, one collection of samples per symbol.

(iii) On collection, we evaluate the upper and lower quartiles[4].

(iv) We calculate the LIV threshold as the mean from the upper and lower quartile of adjacent collections (i.e., H and $\_1$ in Fig. 3), where the lower quartile belongs to the collection containing higher LIVs (H) and the upper quartile belong the other collection pair ($\_1$).

Any new sequence of received LIVs ("apply simulation") is decoded via these thresholds.

5 RESULTS

We evaluate the impact of the distance offset, timing offset, and optimality of the frame selection algorithm using the bit error rate (BER) as a main metric. For each distance and symbol duration, we aim to find a reliable set-up of the aforementioned parameters. Reliable is defined as "BER < 0.01" based on the air-based MC experiments in [8].

We choose $d = 280$ cm as well as the parameters stated in Table 1 to illustrate the impact of distance offset and timing offset. Two different symbol durations with and without a distance offset across different timing offsets have been examined. The timing offset Δt is a relative value meaning the absolute delay is equal to $\Delta t \cdot t_{\mathrm{sym}}$.

In Figures 5 and 6, the BER of $\mathrm{Tx}_{\mathrm{near}}$ and $\mathrm{Tx}_{\mathrm{far}}$ transmission is shown in dependency of a timing offset (Δt) of $\mathrm{Tx}_{\mathrm{far}}$. Negative timing offsets represent delaying $\mathrm{Tx}_{\mathrm{near}}$'s transmission within a

[4]The Rogona simulator offers four different options for how the two values are chosen: *MinMax*, *Quartile*, *Median*, and *Mean*.

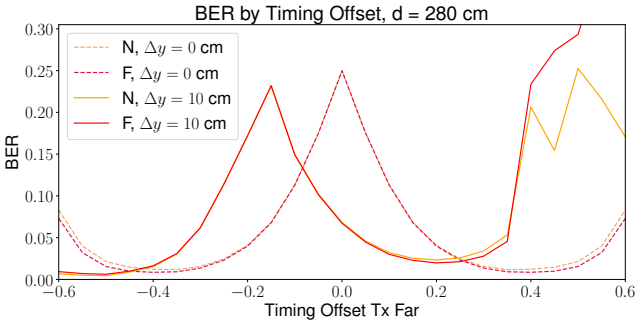

(a) Full

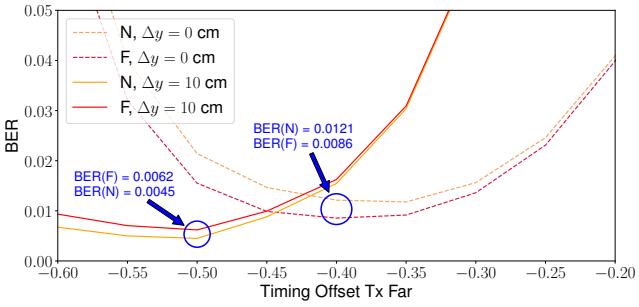

(b) Zoomed in

Figure 5: Mean BER over 300 trials; $t_{\text{sym}} = 75$ ms

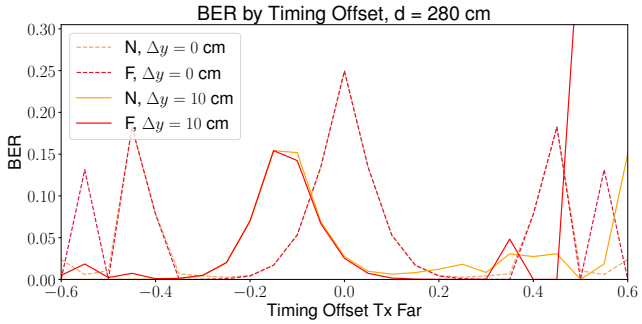

(a) Full

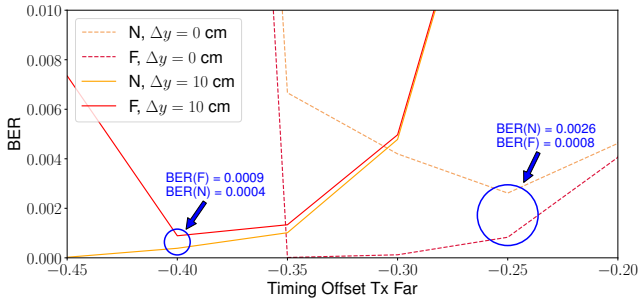

(b) Zoomed in

Figure 6: Mean BER over 300 trials; $t_{\text{sym}} = 100$ ms

symbol duration. The BER is calculated from 300 train-apply pairs in the simulation with a little over 1000 bits per apply.

In Fig. 5a, we observe that the minimum BERs in N and F with positive timing offset are significantly lower at $\Delta t = 0.4$ and $\Delta y = 0$ cm compared to $\Delta t = 0.2$ and $\Delta y = 10$ cm. The BER at $\Delta t = 0.2$ and $\Delta y = 10$ cm is higher, because two effects are working against each other. On the one hand, a distance offset leads to a time shift due to in-/decreased travel duration. This shifts the maximum of the F curve away from the maximum of the N curve. This eventually increases the difference between the already declining N and peaking F, see Fig. 3, thus, reducing the BER. On the other hand, the distance offset also attenuates the F curve, in turn decreasing the difference between declining N and F peak again. The positive timing offset therefore has an advantage compared to a time-shift due to distance offset, as F's amplitude is not attenuated.

The increasing BER we observe in Fig. 5a for $\Delta t = 0.4$, $\Delta y = 10$ cm happens, because simply shifting N and F curves has its limits depending on the steepness of both curves. As soon as they are too far apart, a single sampling point would not suffice to distinguish between $\__1$ and H or $\__2$ and L. In case of distance offset this happens sooner, because of the steepness of the N curve. F and H are then indistinguishable, which leads to a quick rise in BER.

Furthermore, when zooming in on Fig. 5a, depicted in Fig. 5b, we observe that a combination of distance offset and negative timing offset provides even better results than just a timing offset itself. That is, the BER at $\Delta t = -0.5$ and $\Delta y = 10$ cm is less than in the case when $\Delta t = -0.4$ and $\Delta y = 0$ cm.

We also illustrate results for the increased symbol duration of 100 ms, as depicted in Fig. 6. The BER drastically decreases (in a factor of 10^{-1}) compared to the minimum BER in Fig. 5b, but the data-rate also decreases. Nevertheless, arguably more relevant is that a combination of $\Delta y = 10$ cm and negative timing offset leads to the better results in the $t_{\text{sym}} = 100$ ms case as well, see Fig. 6b. In case of negative timing offset combined with a distance offset, several aspects benefit from each other. The slower decline of the F curve helps to separate N and H at the sampling frame, while the N curve is at its maximum thus being distinguishable from the F curve. Furthermore, the faster decline of the N curve and the sooner arrival of Tx_{far} 's transmitters reduces ISI effects. This concludes, that using the distance offset and negative timing offset is a good configuration of the set-up even when a low data-rate is less problematic.

Table 1: Simulation parameters for example case

Parameter	Value
Distance Tx to Tx	280 cm
Distance offset	0, 10 cm
Symbol duration	75 ms, 100 ms
Spray duration	20 ms
Molecules per spray	1000
Rx frame rate	480 FPS
Total of bits	$(144 + 1000) \cdot 300$
Threshold setting method	Quartile

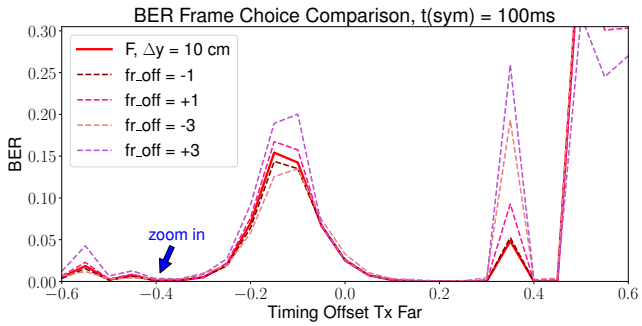

(a) Full

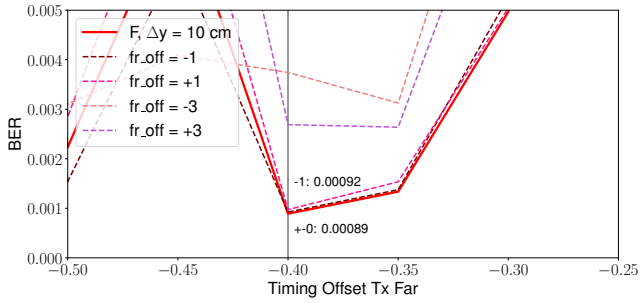

(b) Zoomed in

Figure 7: Comparing different sampling frames

In Fig. 7 we illustrate the optimality of the sampling frame selection algorithm. As an example case, we picked the BER of F at the sampling frame and compared it to selecting −1, 1, −3, and 3 frames across different timing offsets like the experiment in Fig. 6. The here proposed algorithm leads to the minimum BER at the crucial timing offset $\Delta t = -0.4$, as Fig. 7 b).

6 CONCLUSION

We studied the possibility to decode multiple interfering signals in a macroscopic air-based molecular communication system.

In particular, we have shown the significance of a combination of distance offset $\Delta y > 0$ and delaying Tx_{near} 's message $\Delta t < 0$ for ISI reduction and revealing a good sampling point. Through modeling of the CIR according to the probability distribution of the molecules the sampling frame is picked. The selection algorithm and analytical model lead to good BERs across different setups concerning the Tx–Tx distance d, distance offset Δy, and timing offset Δt. The approach of each Tx sending one bit per symbol and Rx receiving two bit per symbol as QCSK leads to a data-rate of 10–20 bit/s (Tx) or 20–40 bit/s (Rx) depending on the Tx–Tx distance and therefore feasible symbol duration. With only one sampling point per symbol and just the LIV as received signal the recorded information size is rather small.

Currently the synchronisation is assumed to be perfect. Depending on the stability of the synchronisation the parameters distance, distance offset, timing offset and eventually more parameters, which have not been explored yet, have to be set with more tolerance. The results have to be further validated with a real-life testbed. This will also provide the possibility to implement an attenuation factor according to the receiver's light saturation level.

ACKNOWLEDGMENT

This work was supported in part by the project MAMOKO funded by the German Federal Ministry of Education and Research (BMBF) under grant number 16KIS0917.

REFERENCES

[1] Mahmoud Abbaszadeh, Weiqiu Li, Lin Lin, Iain White, Petr Denissenko, Peter J. Thomas, and Weisi Guo. 2019. Mutual Information and Noise Distributions of Molecular Signals using Laser Induced Fluorescence. In *IEEE GLOBECOM 2019*. IEEE, Waikoloa, HI, 1–6. https://doi.org/10.1109/GLOBECOM38437.2019.9013877

[2] M. D. Nashid Anjum and Honggang Wang. 2020. Molecular Communication for Wireless Body Area Networks. In *Encyclopedia of Wireless Networks* (1 ed.), Xuemin Shen, Xiaodong Lin, and Kuan Zhang (Eds.). Springer, 921–925. https://doi.org/10.1007/978-3-319-78262-1_152

[3] Iresha Atthanayake, Siavash Esfahani, Petr Denissenko, Ian Guymer, Peter J. Thomas, and Weisi Guo. 2018. Experimental Molecular Communications in Obstacle Rich Fluids. In *ACM NANOCOM 2018*. ACM, Reykjavík, Iceland. https://doi.org/10.1145/3233188.3233216

[4] Sunasheer Bhattacharjee, Martin Damrath, Fabian Bronner, Lukas Stratmann, Jan Peter Drees, Falko Dressler, and Peter Adam Hoeher. 2020. A Testbed and Simulation Framework for Air-based Molecular Communication using Fluorescein. In *ACM NANOCOM 2020*. ACM, Virtual Conference. https://doi.org/10.1145/3411295.3411298

[5] Martin Damrath and Peter Adam Hoeher. 2016. Low-Complexity Adaptive Threshold Detection for Molecular Communication. *IEEE Transactions on NanoBioscience* 15, 3 (Jan. 2016), 200–208. https://doi.org/10.1109/tnb.2016.2520566

[6] Maheshi Buddhinee Dissanayake, Yansha Deng, Arumugam Nallanathan, Maged Elkashlan, and Urbashi Mitra. 2019. Interference Mitigation in Large-Scale Multiuser Molecular Communication. *IEEE Transactions on Communications* 67, 6 (June 2019), 4088–4103. https://doi.org/10.1109/tcomm.2019.2897568

[7] Jan Peter Drees, Lukas Stratmann, Fabian Bronner, Max Bartunik, Jens Kirchner, Harald Unterweger, and Falko Dressler. 2020. Efficient Simulation of Macroscopic Molecular Communication: The Pogona Simulator. In *ACM NANOCOM 2020*. ACM, Virtual Conference. https://doi.org/10.1145/3411295.3411297

[8] Nariman Farsad, Weisi Guo, and Andrew W. Eckford. 2013. Tabletop Molecular Communication: Text Messages through Chemical Signals. *PLOS ONE* 8, 12 (Dec. 2013), 1–13. https://doi.org/10.1371/journal.pone.0082935

[9] Nariman Farsad, H. Birkan Yilmaz, Andrew W. Eckford, Chan-Byoung Chae, and Weisi Guo. 2016. A Comprehensive Survey of Recent Advancements in Molecular Communication. *IEEE Communications Surveys & Tutorials* 18, 3 (2016), 1887–1919. https://doi.org/10.1109/comst.2016.2527741

[10] Werner Haselmayr, Andreas Springer, Georg Fischer, Christoph Alexiou, Holger Boche, Peter Adam Hoeher, Falko Dressler, and Robert Schober. 2019. Integration of Molecular Communications into Future Generation Wireless Networks. In *6G Wireless Summit*. IEEE, Levi, Finland.

[11] Pit Hofmann, Jorge Torres Gómez, Falko Dressler, and Frank H. P. Fitzek. 2022. Testbed-based Receiver Optimization for SISO Molecular Communication Channels. In *IEEE BalkanCom 2022*. IEEE, Sarajevo, Bosnia and Herzegovina, 120–125. https://doi.org/10.1109/BalkanCom55633.2022.9900720

[12] Mehmet Sukru Kuran, H. Birkan Yilmaz, Ilker Demirkol, Nariman Farsad, and Andrea Goldsmith. 2021. A Survey on Modulation Techniques in Molecular Communication via Diffusion. *IEEE Communications Surveys & Tutorials* 23, 1 (Jan. 2021), 7–28. https://doi.org/10.1109/comst.2020.3048099

[13] Mehmet Şükrü Kuran, H. Birkan Yilmaz, Tuna Tugcu, and Ian F. Akyildiz. 2012. Interference effects on modulation techniques in diffusion based nanonetworks. *Elsevier Nano Communication Networks* 3, 1 (March 2012), 65–73. https://doi.org/10.1016/j.nancom.2012.01.005

[14] Rebecca Corinna Pampu. 2023. *Identification of the Signal Source among Multiple Simultaneous Senders in an Air-based Molecular Communication Channel*. Bachelor Thesis. TU Berlin. Advisor(s) Stratmann, Lukas.

[15] Song Qiu, Weisi Guo, Siyi Wang, Nariman Farsad, and Andrew Eckford. 2014. A molecular communication link for monitoring in confined environments. In *IEEE ICC 2014, Workshop on Communications in Underground and Confined Environments*. IEEE, Sydney, Australia. https://doi.org/10.1109/iccw.2014.6881284

[16] Burcu Tepekule, Ali E. Pusane, H. Birkan Yilmaz, Chan-Byoung Chae, and Tuna Tugcu. 2015. ISI Mitigation Techniques in Molecular Communication. *IEEE Transactions on Molecular, Biological and Multi-Scale Communications* 1, 2 (June 2015), 202–216. https://doi.org/10.1109/TMBMC.2015.2501745

[17] Wen-Bin Yang and Kamran Sayrafian-Pour. 2012. Interference Mitigation Using Adaptive Schemes in Body Area Networks. *International Journal of Wireless Information Networks* 19 (2012), 193–200. https://doi.org/10.1007/s10776-012-0192-2